Electronic Supplementary Material (ESI) for Journal of Materials Chemistry A.

Supplementary Information

Pressure-Promoted Irregular $CoMoP_2$ Nanoparticles Activated by Surface Reconstruction for Oxygen Evolution Reaction Electrocatalyst

Shishuai Xu,‡[a,b] *Xiang Gao,*‡[b] *Amol Deshmukh,*‡[c] *Junshuang Zhou,*[d] *Ning Chen,*[e] *Wenfeng Peng,*[b] *Yutong Gong,*[f] *Zhiqiang Yao,*[g] *Kenneth D. Finkelstein,*[h] *Biao Wan,*[a] *Faming Gao,*[c] *Mingzhi Wang,**[a] *Mingyang Chen,**[i,c] *and Huiyang Gou,**[b]

[a] State Key Laboratory of Metastable Materials Science and Technology, Yanshan University Qinhuangdao 066004, China

[b] Center for High Pressure Science and Technology Advanced Research, Beijing 100094, China

[c] Computational Science Research Center, Beijing, 100193, China

[d] College of Environment and Chemical Engineering, Yanshan University, Qinhuangdao 066004, China

[e] Canadian Light Source, Saskatoon, SK, CAN S7N 0X4, Canada

[f] International Center for Materials Discovery, School of Materials Science and Engineering, Northwestern Polytechnical University, Xi'an, Shanxi 710072, (China)

[g] School of Materials Science and Engineering, Zhengzhou University, Zhengzhou 10459, China

[h] Cornell High Energy Synchrotron Source (CHESS), Cornell University, New York 14853, United States

[i] Center for Green Innovation, School of Materials Science and Engineering, University of Science and Technology Beijing, Beijing 100083, China

Corresponding Authors

*E-mail for H.G: huiyang.gou@gmail.com

*E-mail for M.C: mychen@ustb.edu.cn

*E-mail for M.W: wmzw@ysu.edu.cn

Experimental Section

Materials. Cobalt powder (purity, > 99.99%; diameter, ~60 nm), molybdenum powder (purity, > 99.99%; diameter, 60 ~ 200 nm) and red phosphorus (purity, > 99.999%; diameter, 1 ~ 5 mm) were purchased from Aladdin Chemical Co., Ltd. Potassium hydroxide (KOH, AR; density, 2.130 $g\cdot cm^{-2}$) and Nafion (D-521) were purchased from Tianjin Komiou Chemical Reagent Co., Ltd. All the materials were used without any further purification in this experiment.

Synthesis of bulk bimetallic phosphides ($CoMoP_2$). The bulk bimetallic phosphide was synthesized mainly through high pressure annealing process in cubic multi-anvil system (CS-1B type, Guilin, China). The standard COMPRES assembly was consisted of cubic pyrophyllite, graphite crucibles heater and an h-BN capsule thermal insulator, and the assembly schematic is presented in **Scheme 1**. Temperature and power curves (T–P Curves) were calibrated using W-Re (type C) thermocouples. Firstly, the mixture with mole ratio of 1:1:2 (Co:Mo:P) for $CoMoP_2$ was prepared in a glove box (Ar atmosphere, O_2&H_2O <0.1 ppm). Subsequently, the mixtures were pre–pressed into a cylindrical block precursor (Ø 6.8 mm × 3 mm) at ~20 MPa, and encapsulated into an hBN capsule. Finally, the standard COMPRES assembly was treated at

1500 °C for 5 min under 5.0 GPa followed by cooling to room temperature quickly. The product was peeled out from the COMPRES assembly, and ultra-washed by deionized water for several times, and then dried in the air. For comparison, CoP_2 and MoP_2 were synthesized as the same condition as bulk of $CoMoP_2$. The irregular $CoMoP_2$ nanoparticles were obtained through ball-milled method. All the samples were ball-milled using a planetary type high energy ball mill with the ball to power ratio of 20:1 at 350 rpm for 10 h under Ar atmosphere.

Characterizations. The morphology structure was characterized by field emission scanning electron microscope (FESEM, Japan, Type S4800) and transmission electron microscopy (TEM&HRTEM, JEOL2010, Japan), equipped with energy dispersive spectrometer (EDS). The crystal structure was checked by X-ray diffraction (XRD, DMAX-2500, Japan) with Cu Kα radiation source (λ = 1.5406 Å, 40 kV, 200 mA) at a scan rate of 2° min^{-1}. The chemical states of the elements were characterized by X−ray photoelectron spectroscopy (XPS, AXIS Ultra DLD, Japan) with a monochromatic Al Kα X−ray source, and the binding energy was calibrated with the C 1s peak at 284.6 eV taken as an internal standard. The XANFS were performed using Hard X-ray Micro-Analysis (HXMA) beamline Light Source in Canadian (CLS) and Cornell High Energy Synchrotron Source (CHESS) in United States, and the storage ring was operated at 250 mA mode with a Si (111) double crystal monochromator. The energy calibrations were carried out according to Co (7709 eV). All XAS spectra fittings were conducted by the ATHENA module of IFEFFIT software packages.[1]

Electrochemical measurements. All the electrochemical measurements were recorded on CHI 760e electrochemical analyzer (Chenhua, Shanghai) using a standard three-electrode system under room temperature. Cyclic voltammetry (CV) and linear sweep voltammetry (LSV) measurements were performed in 1.0 M KOH electrolyte without iR compensation. The glassy carbon electrode (AFE5050GC, Ø 5 mm), Hg&HgO (3.5 mol·L^{-1} KCl solution) and an Pt/C piece (1 cm × 1 cm) served as working electrode, reference electrode (RE), and counter electrodes (CE), respectively. The 10 μl of catalyst ink was applied on the GC electrode with catalyst loading of ~ 0.255 mg·cm^{-2} for all samples. Cyclic voltammograms (CV) were tested in the region of 1.1−1.2 V (vs. RHE) with various scan rates (5−80 mV·s^{-1}). The catalysts were cycled 5 times at scan rate of 50 mV·s^{-1} to obtain stable LSV curves, then OER polarization curves were obtained in a N_2-saturated 1.0 mol·L^{-1} KOH solution at a scan rate of 5 mV·s^{-1} with the RDE at 1600 rpm. Electrochemical impedance spectroscopy (EIS) was performed at 0.52 (vs. SCE) in a frequency range from 100 kHz to 0.01 Hz. Chronoamperometric test was conducted at the constant current density of 10 mA·cm^{-2}. In all measurements, the HgO reference electrode was calibrated to the reversible hydrogen electrode (RHE) on the basis of Nernst equation (1):[2]

$$\mathrm{R(RHE)} = \mathrm{E(Hg/HgO)} + 0.098 + 0.095 \times \mathrm{pH} \tag{1}$$

The turnover frequency (TOF) was calculated as shown in equation (2).[3]

$$\mathrm{TOF} = \frac{\mathrm{J} \times \mathrm{A}}{4 \times \mathrm{F} \times \mathrm{n}} \tag{2}$$

where J is the current density (at 1.5 V *vs.* RHE), F is the Faraday constant (96485.3 C/mol) and n is the mole number of the total catalyst.

$$\mathrm{FE} = \frac{\mathrm{I_R}}{\mathrm{I_D N}}$$

(3)

where I_R and I_D are current obtained by rotating disk electrode at potential of 0.3 V (*vs.* RHE), and N is current collection efficiency.

Computational Details. All of the first-principles calculations in this study were performed at density functional theory (DFT) level using Vienna Ab-initio Simulation Package (VASP).[4,5]

The exchange correlation energies were approximated by using the Perdew, Burke, and Ernzerhof (PBE) functional.[6] The spin-polarized wavefunction of valence electrons were expanded in plane wave basis sets with a cutoff energy of 400 eV. The pseudopotentials were constructed with the projected augmented wave (PAW) method.[7,8] The Grimme DFT-D_3 method is applied to correct the dispersion interactions.[9] For bulk systems, the positions of the atoms were optimized until the forces on each atom were below 0.01 eV/Å with the lattice parameters also being relaxed. For the slab calculations, the lattice parameters of the optimized bulk systems were used and only the positions of the atoms were optimized. A vacuum of at least 15 Å was set for all the slab systems.

OER reactions over the (001) and (104) surfaces of $CoMoP_2$ were modelled using a slab structural model. Additional systems such as the (104) slab of $NiMoP_2$ were investigated similarly. The (104) slab was cut from the crystal structure of $CoMoP_2$ with a thickness of ~7.5 Å. The (104) slab unit cell has a narrow shape with a surface area of 15.84×3.26 Å^2, so a 1× 3 supercell and a 1 × 2 k-point mesh were used in the DFT calculation. The (001) slab unit cell has a thickness of 11.10 Å and a surface area of 3.26×6.53 Å^2, and a 4 × 4 supercell was used with a 2 × 2 k-point mesh. The active sites on the slabs are determined by comparing the OH adsorption energies at different surface sites using OH as a probe. The OER reaction was modelled for the selected active sites, following the 4-electron (or 4-hole) mechanism proposed by Nørskov.[10,11]

$$\mathrm{OH^- + * \rightarrow *OH + e^-} \quad (4)$$

$$\mathrm{*OH \rightarrow *O + H^+ + e^-} \quad (5)$$

$$\mathrm{OH^- + *O \rightarrow *OOH + e^-} \quad (6)$$

$$\mathrm{*OOH \rightarrow * + O_2 + H^+ + e^-} \quad (7)$$

where the adsorbates including OH, O, and OOH are added to the active site of the slabs (*) and the reaction energies were calculated accordingly. Energy of O_2 is difficult to correctly determine using plane wave DFT, so the reaction energy for step (6) was determined based on the experimental reaction energy of 4.92 eV.[12,13] The reaction Gibbs free energy can be obtained by correcting the reaction energies with calculated zero-point energy and experimental entropy corrections.[14] The zero-point energies were calculated by summing up the vibrational frequencies obtained from normal mode analysis using harmonic approximation. The zero-point energy and entropy corrections, in total, will normally change the reaction energy for an elementary step by less than 0.2 eV. Since the total correction is a small value yet the computation being expensive, we only included the corrections for more important systems (OER on Co of oxidized $CoMoP_2$ and on Ni of oxidized $NiMoP_2$).

The work functions for the slabs of a series of phosphides were predicted at DFT level with PBE function. The work functions were calculated as the difference between the vacuum and the Fermi level from the VASP calculation. This is because the Fermi level calculated using VASP is arbitrary, and needs to be shifted based on the calculated vacuum potential which is non-zero, so that the vacuum energy level is set to zero. The vacuum potential is determined by converging the planar average of the electrostatic potential at a distance from the slab. The work function is predicted as the negative of the Fermi energy with respect to vacuum at zero. MoP (011), CoP (011), $CoMoP_2$ (104), and slabs of the $CoMoP_2$-like systems including $MoMoP_2$ (104), $NiMoP_2$ (104) and $CoCoP_2$ (104) were built and optimized with fixed lattice parameters (their lattice parameters are taken from the optimized bulk systems). It is noted that the c value of $CoMoP_2$ is about 4 times of the c value of MoP while the $CoMoP_2$ unit cell is approximately a 4-stack of the MoP_2 unit cell, so the MoP (011) is actually the analogous surface for the $CoMoP_2$ (104)

surface, although they actually appear different due to the additional inversion symmetry in $CoMoP_2$. The (104) surfaces for MoP and CoP are not smooth, and their surface energy are expected to be too high for surface termination for OER.

Table S1. Chemical compositions detected by energy dispersive spectroscopy (EDS).

Samples	Elements	Weight (wt %)	Atom (at %)
$CoMoP_2$	P K	30.30	52.57
	Co K	23.81	22.72
	Mo L	45.89	24.71
MoP_2	P K	38.91	66.36
	Mo L	61.09	33.64
CoP_2	P K	66.84	65.73
	Co L	33.16	34.27

Table S2. Comparison of the catalytic activity toward the oxygen evolution reaction of $CoMoP_2$ irregular nanoparticles with other reported catalysts.

Catalysts	Overpotential (at $10mA\cdot cm^{-2}$)	Tafel slope ($mV\cdot dec^{-1}$)	Stability	Refers
Irregular $CoMoP_2$ nanoparticles	270	51	20 h/6000 cycles	This work
Mn-Co oxyphosphide	320	52	8 h	15
tannin-NiFe (TANF) complex	290	28	2000 cycles	16
CoP/PNC	300	77	20 h/1000 cycles	17
$Ni_{2-x}Ru_xP$ particles	340	/	20 h/300 cycles	18
α-$Co(OH)_2$ nanomeshes	300	69	~5.5 h	19
Few-layer BP	>400	75	~2.8 h	20
FeP@GPC	278	/	20 h/3000 cycles	21
NiCoP/C nanoboxes.	330	96	10 h	22
N-NPO/CC	270	102	100 h	23
M-Co_3O_4/NPC	300	83	10 h	24
Co-P/Co-N-C/NPC	370	92	~13.9 h	25
$Co_{0.6}Fe_{0.4}P$	300	48	120 h/5000 cycles	26
Multishelled Ni_2P	270	40	20 h	27
NiFeP@NPC	350	78	20 h/1000	28
$Co_{0.9}S_{0.58}P_{0.42}$	270	/	20 h/3000 cycles	29
Co_2P nanosheets	280	66.5	48 h	30
CoP/NCNHP	310	70	19 h/1000 cycles	31
CoP/C	330	53	25 h	32
Co-P@PC-750	283	53	20 h	33

Table S3. Structural parameters extracted from the converted Fourier transform (FT) in R space.

Catalysts	Shell	CN[a]	R_j (Å)[b]	σ^2(×10^3) (Å^2)[c]	ΔE_0(eV)[d]	*R*-factor
$CoMoP_2$ before	Co-P1	6	2.26	0.0057	-2.80	0.002
	Co-Mo1	2	2.82	0.0100	-2.80	0.002
	Co-Co1	3	3.32	0.0090	-2.80	0.002
	Co-P2	4	4.17	0.0050	-2.80	0.002
	Co-Mo2	5	4.37	0.0050	-2.80	0.002
$CoMoP_2$ after OER	Co-O1	2	1.90	0.0066	-5.31	0.002
	Co-P1	4	2.24	0.0050	-5.31	0.002
	Co-Mo1	2	3.07	0.0063	-5.31	0.002
	Co-Co1	6	3.43	0.0099	-5.31	0.002
	Co-O2	6	3.58	0.0073	-5.31	0.002
	Co-P2	6	3.99	0.0090	-5.31	0.002
$CoMoP_2$ $P6_3/mmc$	Co-P1	6	2.26	Reference 34		
	Co-Mo1	2	2.83			
	Co-Co1	6	3.30			

[a] CN: Coordination No.; CN was fixed during fitting; [b] R_j: bonding distance; [c] σ^2: Debye-Waller factor; [d] ΔE_0: inner potential shift.

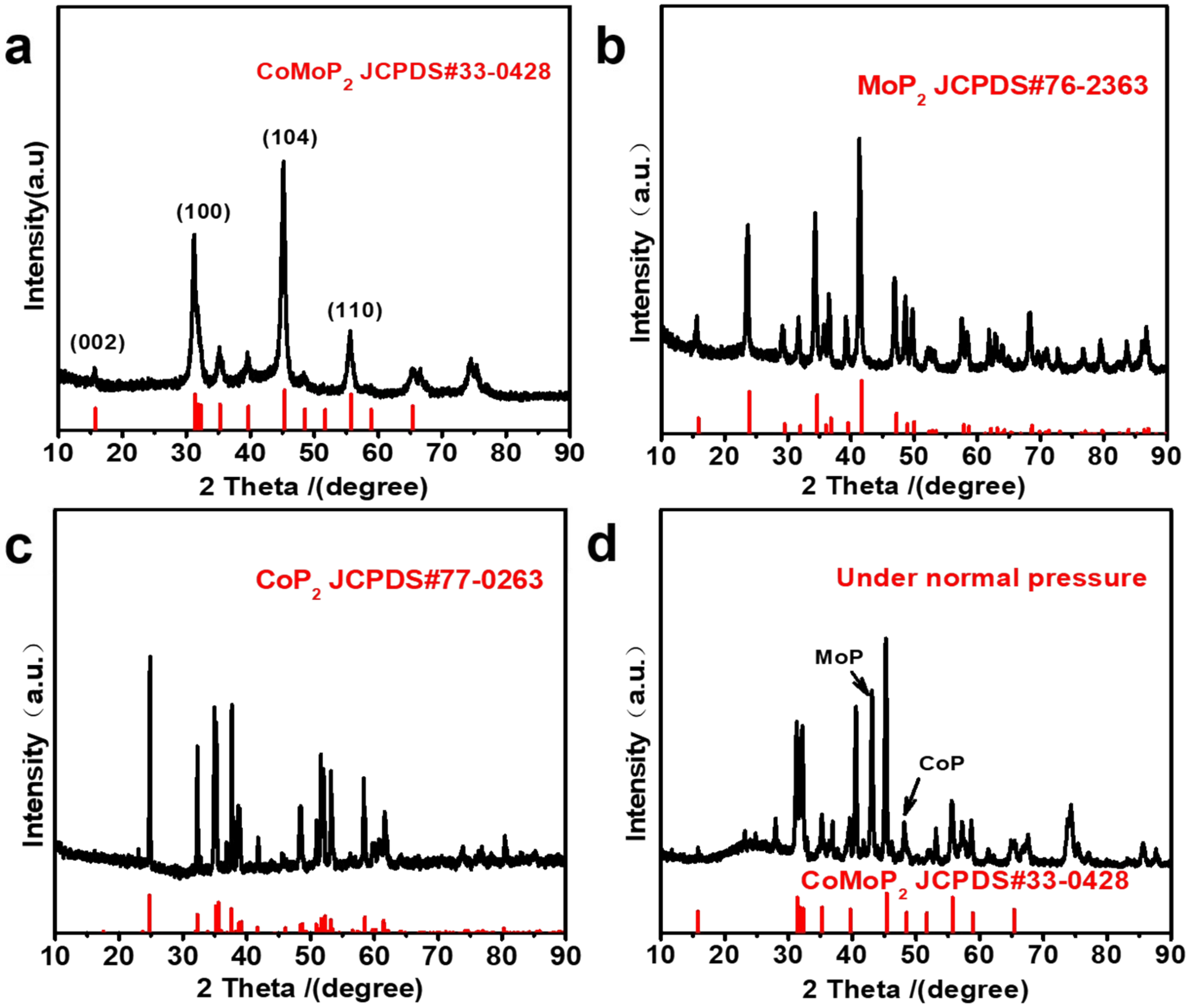

Figure S1. XRD pattern for (a) $CoMoP_2$, (b) MoP_2 and (c) CoP_2. (d) the XRD pattern of sample is obtained as the same annealing conditions as the $CoMoP_2$, except for normal pressure.

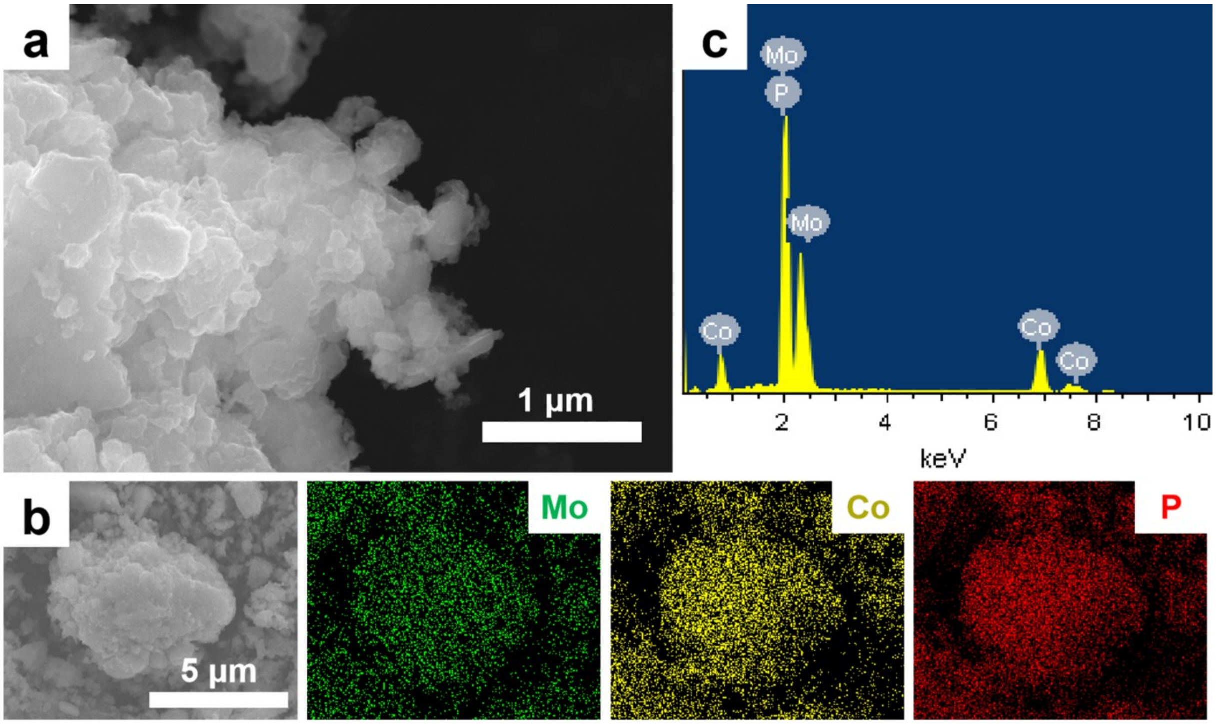

Figure S2. SEM of (a) $CoMoP_2$ and (b) corresponding EDS elemental mapping. (c) FESEM−EDS spectrum.

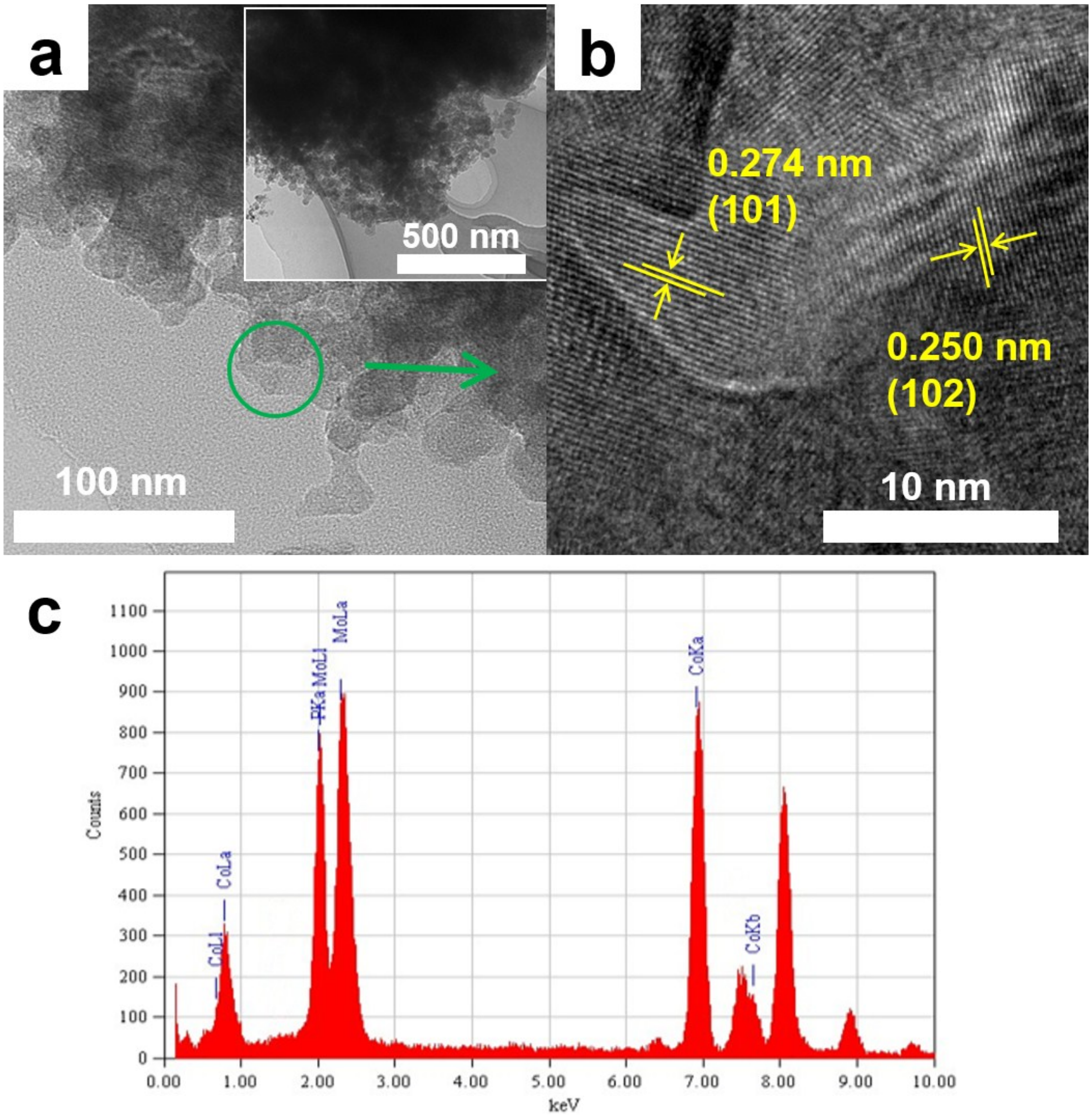
a
500 nm
100 nm
b
0.274 nm
(101)
0.250 nm
(102)
10 nm
c
Counts
keV
CoLl
CoLa
PKa MoLl
MoLa
CoKa
CoKb
0
100
200
300
400
500
600
700
800
900
1000
1100
0.00
1.00
2.00
3.00
4.00
5.00
6.00
7.00
8.00
9.00
10.00

Figure S3. (a) Transmission electron microscopy (TEM) image of $CoMoP_2$ (Inset: Low magnification TEM image), and (b) cross-section HRTEM image and (c) corresponding elemental spectrum of Co, Mo and P.

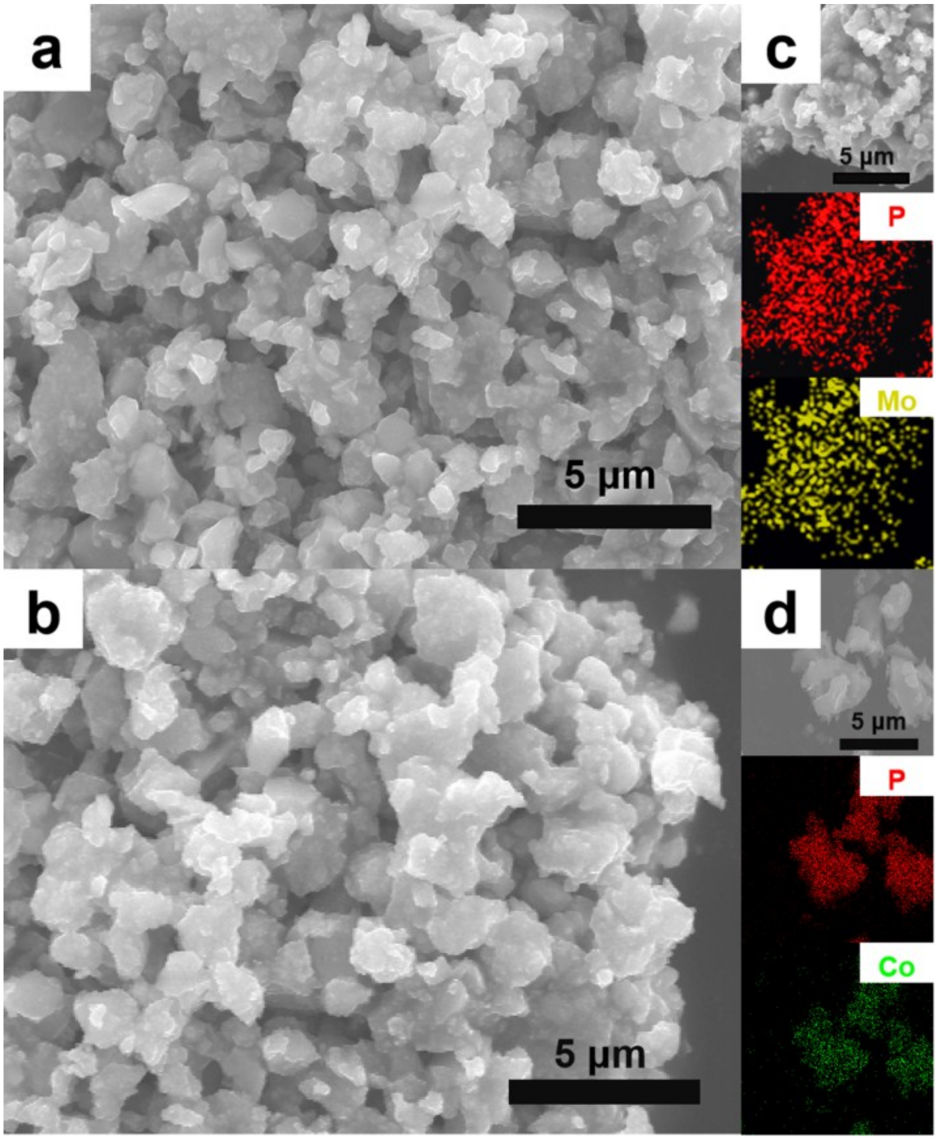

Figure S4. SEM images of (a) MoP_2 and (b) CoP_2. The corresponding EDS elemental mapping of Co, Mo and P for (c) MoP_2 and (d) CoP_2, respectively.

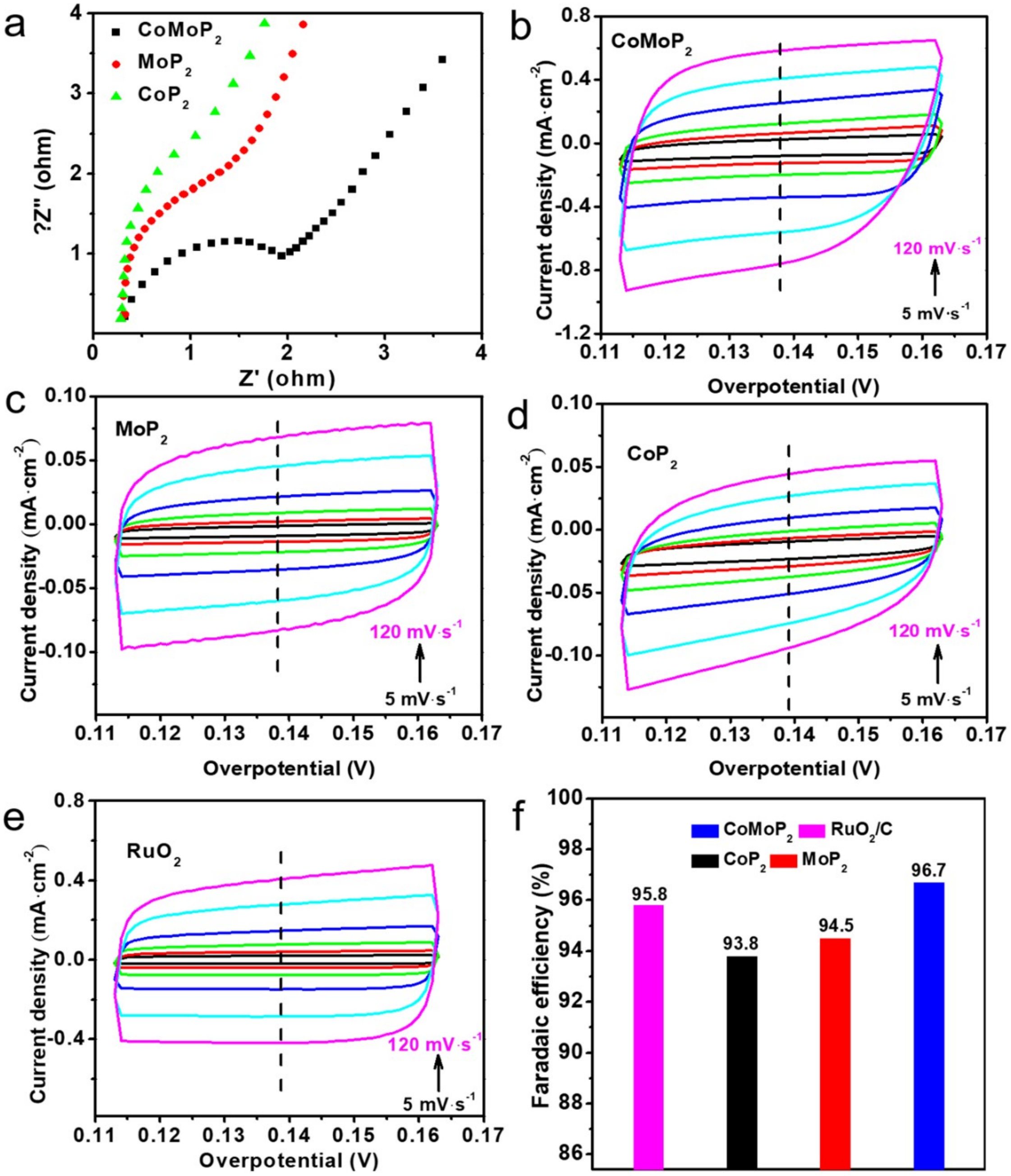

Figure S5. (a) EIS Nyquist plots of various catalysts, tested at 360 mV overpotential. Cyclic voltammetry cycles of (b) $CoMoP_2$, (c) MoP_2, (d) CoP_2 and (e) RuO_2 in an overpotential windows of 110−160 mV with different scan rates. (f) Faradaic efficiency of $CoMoP_2$, RuO_2/C, CoP_2 and MoP_2 are calculated in 1.0 M KOH.

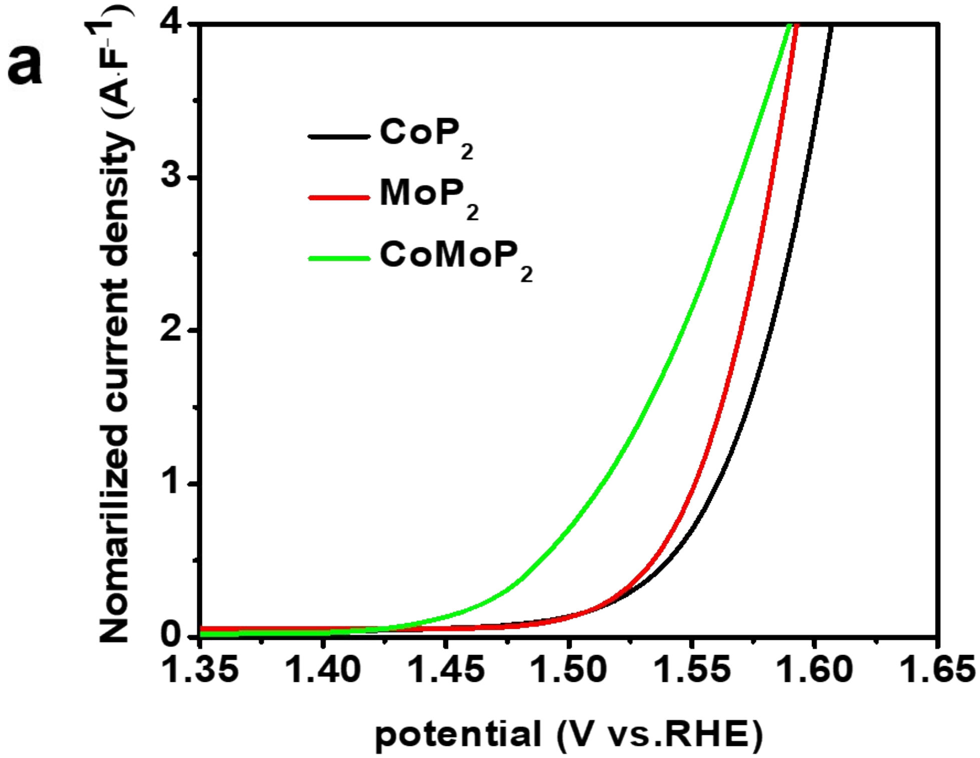

Figure S6. (a) The LSV curves normalized by the Cdl values.

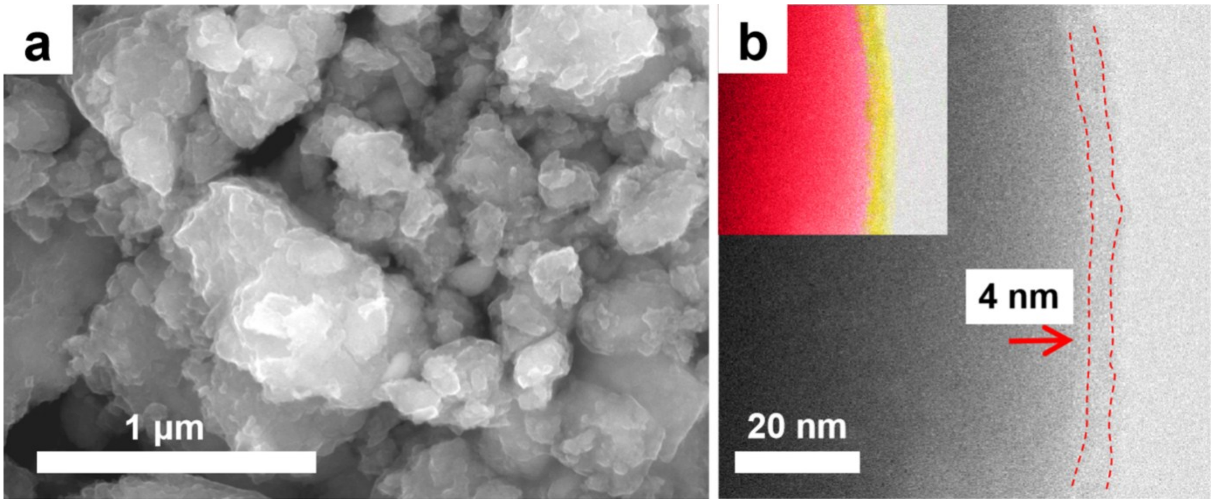

Figure S7. (a) SEM image and (b) low magnification TEM image for $CoMoP_2$ after OER.

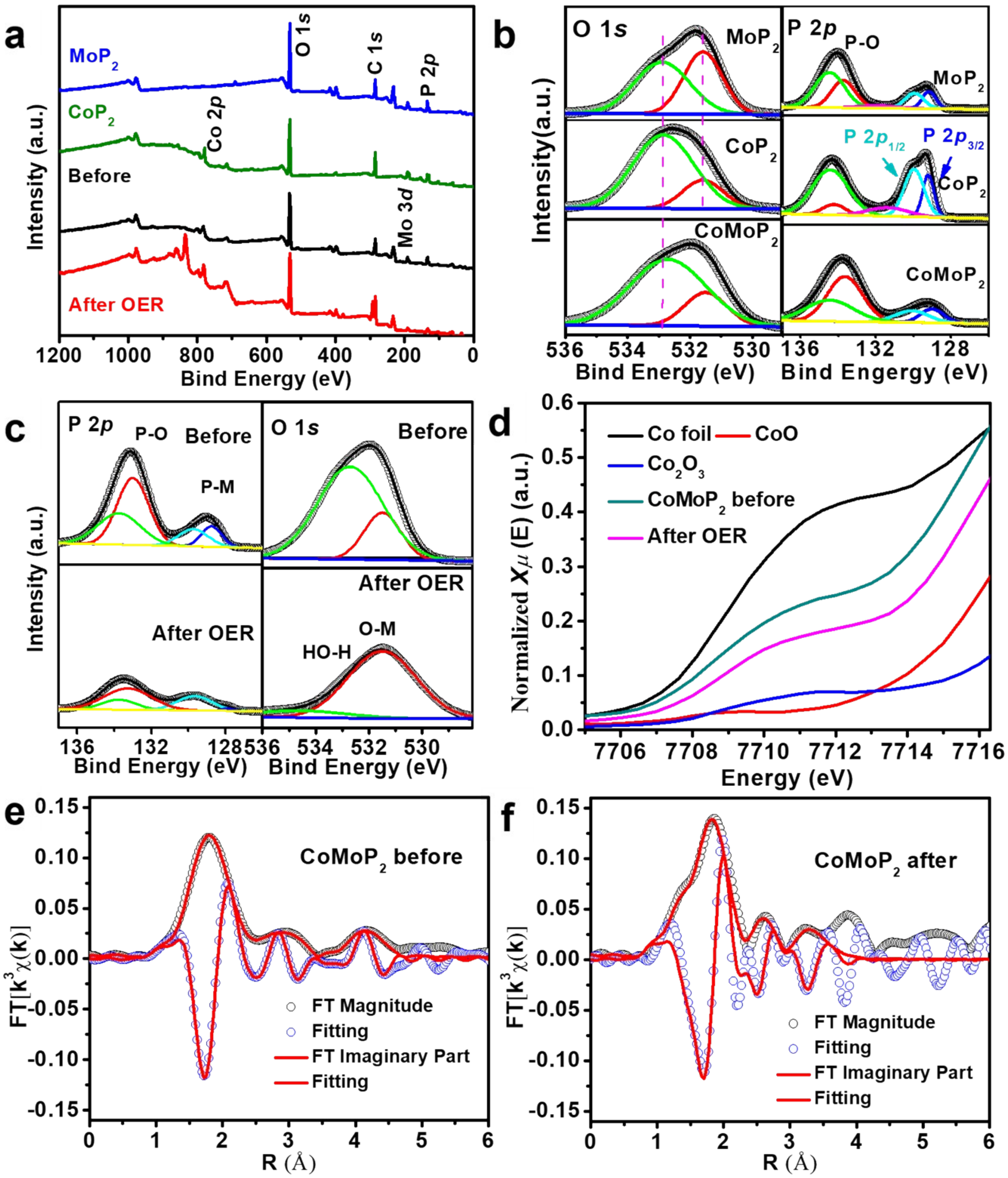

Figure S8. (a) XPS survey spectra for all samples. (b) High-resolution XPS spectra of O 1s and P 2p for MoP_2, CoP_2, $CoMoP_2$ before. (c) XPS spectra of P 2p and O 1s for $CoMoP_2$ after OER compared with before. "Sat." indicates satellite peaks. (d) The magnified XANES spectra at Co pre-edge region of Co foil, CoO, Co_2O_3, $CoMoP_2$ before and after OER. (e) and (f) Fourier transformed EXAFS fitting curves of $CoMoP_2$ before and after OER.

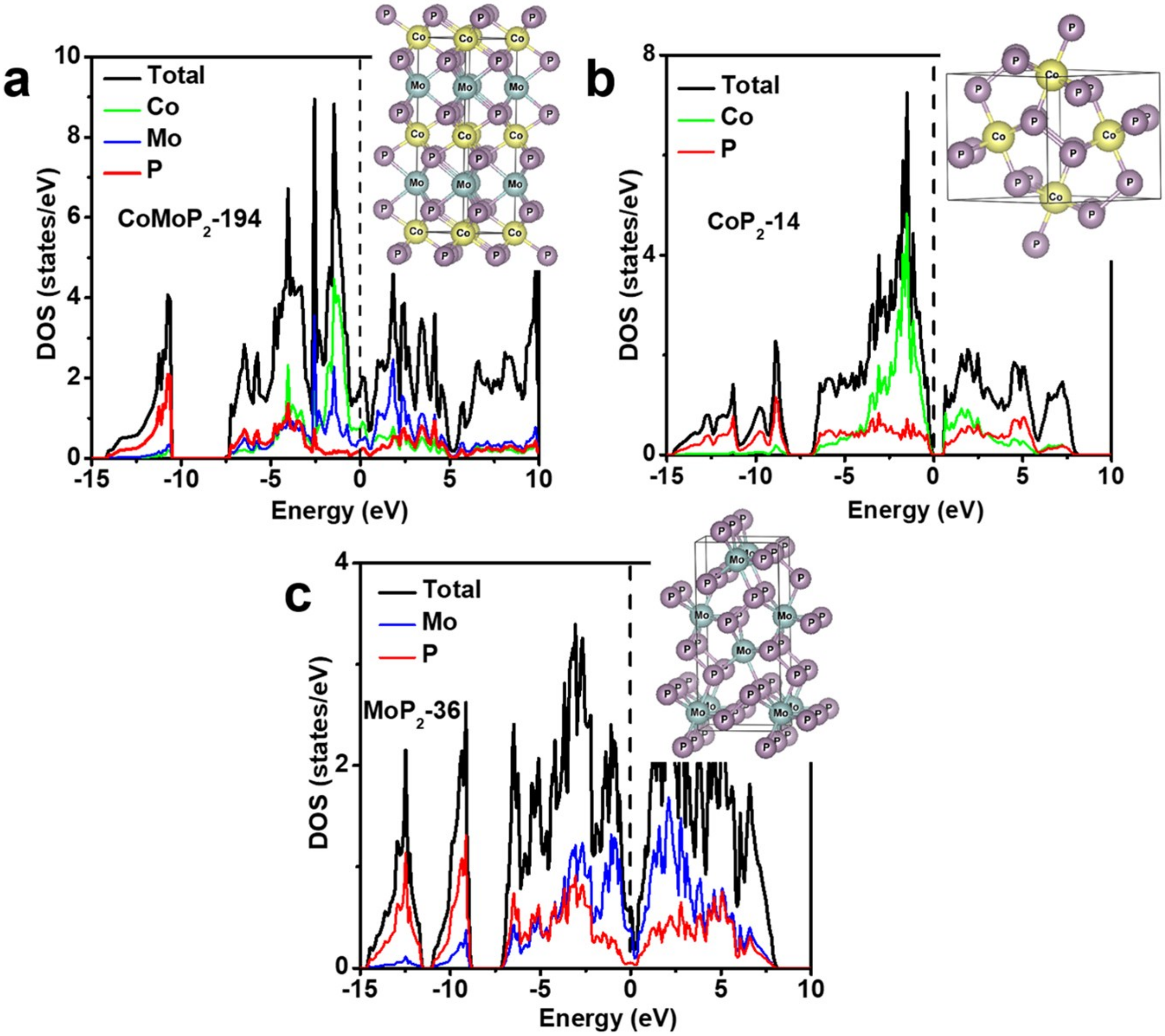

Figure S9. Density functional theory calculations (DOS) of (a) $CoMoP_2$, (b) CoP_2 and (c) MoP_2 with side view crystal cell (inset).

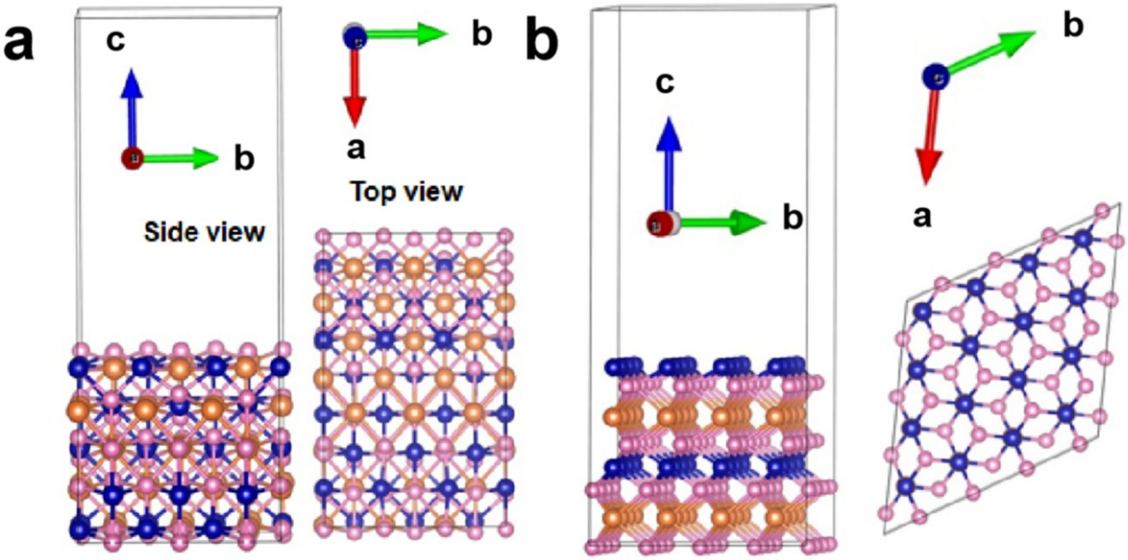

Figure S10. Atomistic structures for the (a) (104) and (b) (001) surfaces of $CoMoP_2$. Blue = Co, orange = Mo, pink = P.

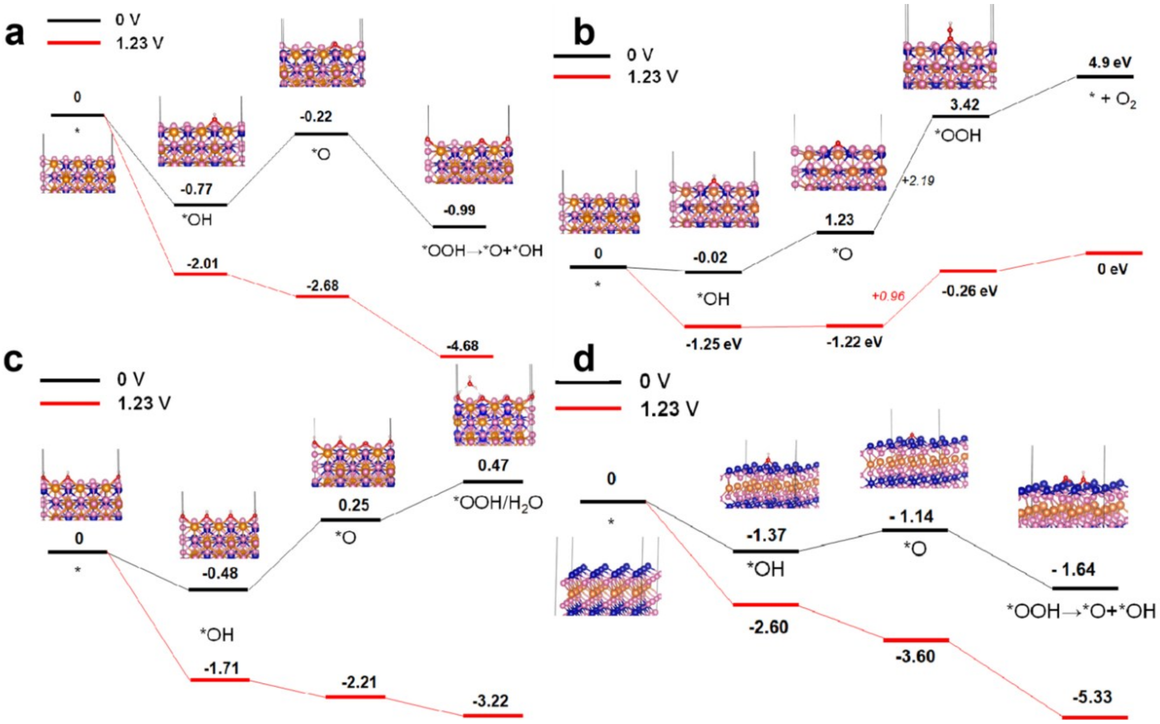

Figure S11. Predicted OER energy profile for OER at (a) Mo site and (b) Co site of clean $CoMoP_2$ (104) surface, (c) Mo site of partially oxidized $CoMoP_2$ (104) surface, and (d) Mo site of clean $CoMoP_2$ (001) surface at the PBE level. Blue = Co, orange = Mo, pink = P.

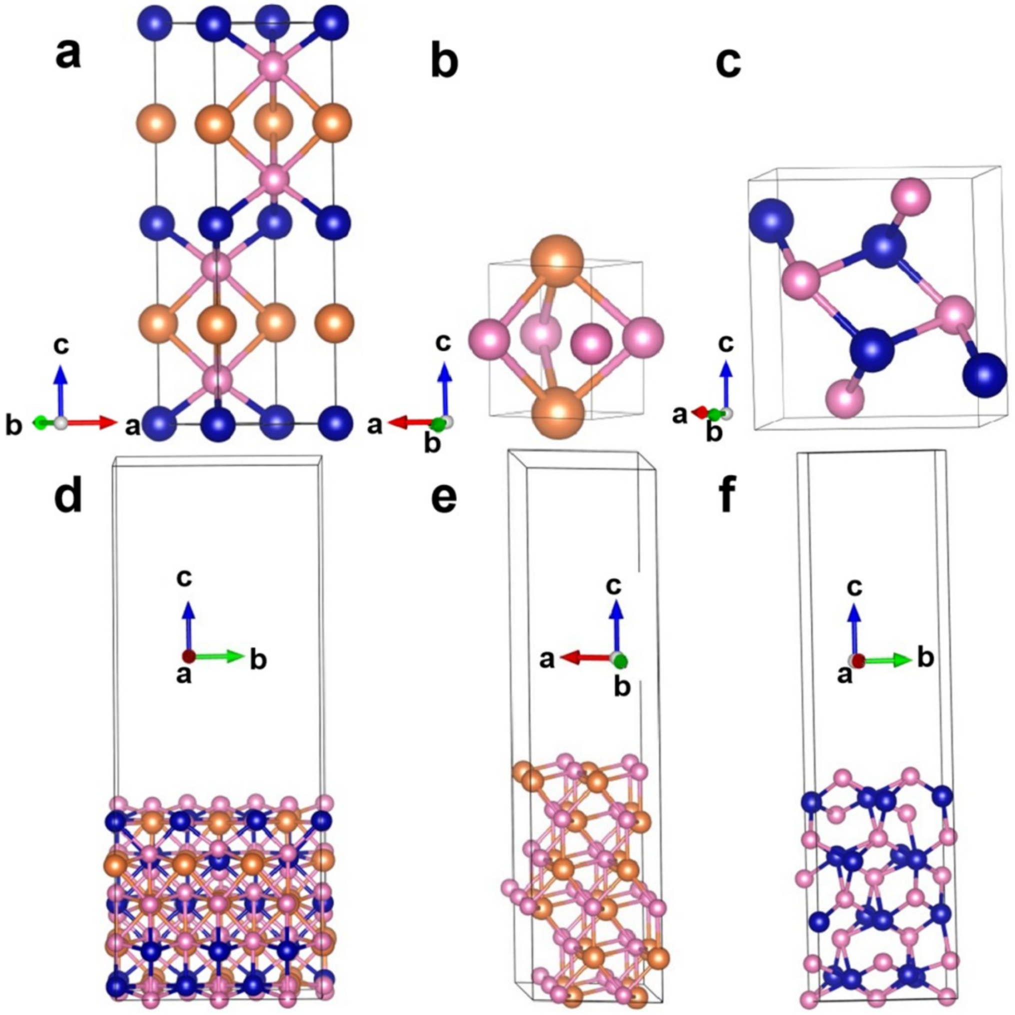

Figure S12. Illustration of crystal structures for (a) $CoMoP_2$ (b) MoP and (c) CoP. Constructed slabs for (d) $CoMoP_2$ (104), (e) MoP (011) and (f) CoP (011). Blue = Co, orange = Mo, pink = P.

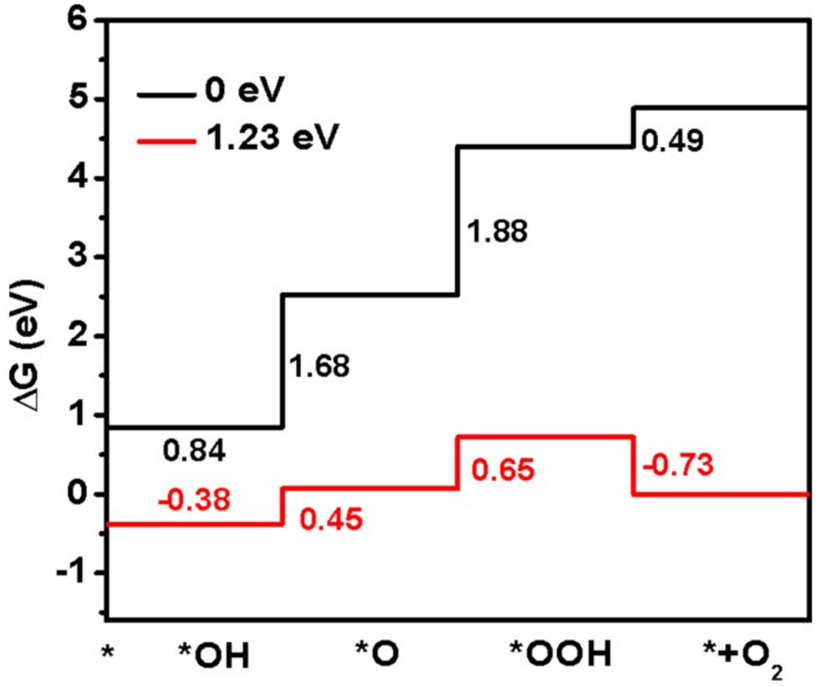

Figure S13. Predicted OER energy profile for OER at Ni site of partially oxidized $NiMoP_2$ (104) surface at the PBE level.

References

1. B. Ravel, M. Newville, *Synchrotron Rad.*, 2005, **12**, 537–541.

2. B. Zhang, X. Zheng, O. Voznyy, R. Comin, M. Bajdich, M. G. Melchor, L. Han, J. Xu, M. Liu, L. Zheng, F. P. G. Arquer, C. T. Dinh, F. Fan, M. Yuan, E. Yassitepe, N. Chen, T. Regier, P. Liu, Y. Li, P. D. Luna, A. Janmohamed, H. L. Xin, H. Yang, A. Vojvodic, E. H. Sargent, *Science*, 2016, **352**, 333–337.

3. Z. Zou, T. Wang, X. Zhao, W. J. Jiang, H. Pan, D. Gao, C. Xu, *ACS Catal.,* 2019, **9**, 7356−7364.

4. G. Kresse, J. Furthmüller, Comput. *Mater. Sci.*, 1996, **6**, 15–50.

5. G. Kresse, J. Furthmüller, *Phys. Rev. B,* 1996, **54**, 11169–11186.

6. J. P. Perdew, K. Burke, M. Ernzerhof, *Phys. Rev. Lett.* 1996, **77**, 3865–3868.

7. G. Kresse, D. Joubert, *Phys. Rev. B,* 1999, **59**, 1758–1775.

8. P. E. Blöchl, *Phys. Rev. B,* 1994, **50**, 17953–17979.

9. S. Grimme, S. Ehrlich, L. Goerigk, *J. Comput. Chem.* 2011, **32**, 1456–1465.

10. J. Rossmeisl, A. Logadottir, J. K. Nørskov, *Chem. Phys.* 2005, **319**, 178–184.

11. J. Rossmeisl, Z. W. Qu, H. Zhu, G. J. Kroes, J. K. Nørskov, *J. Electrochem. Soc.* 2007, **607**, 83–89.

12. J. K. Nørskov, J. Rossmeisl, A. A. Logadottir, L. Lindqvist, J. R. Kitchin, T. Bligaard, H. Jonsson, *J. Phys. Chem. B,* 2004, **108**, 17886–17892.

13. K. Srinivasu, S. K. Ghosh, *J. Phys. Chem. C,* 2013, **117**, 26021–26028.

14. J. K. Nørskov, T. Bligaard, A. Logadottir, J. R. Kitchin, J. G. Chen, S. Pandelov, U. Stimming, *J. Electrochem. Soc.,* 2005, **152**, J23–J26.

15. B. Y. Guan, L. Yu, X. W. D. Lou, *Angew. Chem. Int. Ed.,* 2017, **56**, 2386–2389.

16. Y. Shi, Y. Yu, Y. Liang, Y. Du, B. Zhang, *Angew. Chem. Int. Ed.,* 2019, **58**, 3769–3773.

17. Z. Peng, Y. Yu, D. Jiang, Y. Wu, B. Y. Xia, Z. Dong, *Carbon,* 2019, **144**, 464–471.

18. D. R. Liyanage, D. Li, Q. B. Cheek, H. Baydouna, S. L. Brock, *J. Mater. Chem. A,* 2017, **5**, 17609–17618.

19. B. Zhang, J. Zhang, X. Tan, D. Tan, J. Shi, F. Zhang, L. Liu, Z. Su, B. Han, L. Zheng, *Chem. Commun.* 2018, **54**, 4045–4048.

20. X. Ren, J. Zhou, X. Qi, Y. Liu, Z. Huang, Z. Li, Y. Ge, S. C. Dhanabalan, J. S. Ponraj, S. Wang, *Adv. Energy Mater.,* 2017, **7**, 1700396.

21. Y. Yao, N. Mahmood, L. Pan, G. Shen, R. Zhang, R. Gao, F. Aleem, X. Yuan, X. Zhang, J. Zou, *Nanoscale,* 2018, **10**, 21327–21334.

22. P. He, X. Y. Yu, X. W. Lou, *Angew. Chem. Int. Ed.,* 2017, **56**, 3897–3900.

23. J. Huang, Y. Sun, Y. Zhang, G. Zou, C. Yan, S. Cong, T. Lei, X. Dai, J. Guo, R. Lu, *Adv. Mater.,* 2018, **30**, 1705045.

24. X. Yang, J. Chen, Y. Chen, P. Feng, H. Lai, J. Li, X. Luo, *Nano-Micro Lett.,* 2018, **10**, 15, 2311-6706.

25. S. Wang, H. Jang, J. Wang, Z. Wu, X. Liu, J. Cho, *ChemSusChem,* 2019, **12**, 830–838.

26. Y. Lian, H. Sun, X. Wang, P. Qi, Q. Mu, Y. Chen, J. Ye, X. Zhao, Z. Deng, Y. Peng, *Chem. Sci.,* 2019, **10**, 464–474.

27. H. Sun, X. Xu, Z. Yan, X. Chen, F. Cheng, P. S. Weiss, J. Chen, *Chem. Mater.,* 2017, **29**, 8539–8547.

28. J. Wang, F. Ciucci, *Appl. Catal. B-Environ.*, 2019, **254**, 292-299.

29. Z. Dai, H. Geng, J. Wang, Y. Luo, B. Li, Y. Zong, J. Yang, Y. Guo, Y. Zheng, X. Wang, Q. Yan, *ACS Nano,* 2017, **11**, 11031–11040.

30. Z. Pan, P. Niu, Y. Hou, Y. Fang, M. Liu, X. Wang, *ChemSusChem,* 2019, **12**, 1911–1915.

31. Y. Pan, K. Sun, S. Liu, X. Cao, K. Wu, W. Cheong, Z. Chen, Y. Wang, Y. Li, Y. Liu, *J. Am. Chem. Soc.,* 2018, **140**, 2610–2618.

32. Y. J. Bai, H. J. Zhang, Y. Y. Feng, L. Fang, Y. Wang, *J. Mater. Chem. A*, 2016, **4**, 9072-9079.

33. J. Wu, D. Wang, S. Wan, H. Liu, C. Wang, X. Wang, *Small*, 2019, 1900550.

34. A. Jain, S. P. Ong, G. Hautier, W. Chen, W. D. Richards, S. Dacek, S. Cholia, D. Gunter, D. Skinner, G. Ceder, K. A. Persson, *APL Mater.,* 2013, **1**, 011002.